Thickness-dependent terahertz emission from Bi_2S_3 films under excitation below and above the band gap

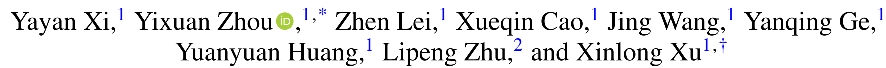

Yayan Xi,[1] Yixuan Zhou,[1,*] Zhen Lei,[1] Xueqin Cao,[1] Jing Wang,[1] Yanqing Ge,[1]
Yuanyuan Huang,[1] Lipeng Zhu,[2] and Xinlong Xu[1,†]

[1]*Shaanxi Joint Lab of Graphene, Laboratory of Photon-Technology in Western China Energy, International Collaborative Center on Photoelectric Technology and Nano Functional Materials, Institute of Photonics & Photon-Technology, School of Physics, Northwest University, Xi'an 710069, China*

[2]*School of Electronic Engineering, Xi'an University of Posts and Telecommunications, Xi'an 710121, China*

(Received 7 September 2022; revised 9 January 2023; accepted 10 January 2023; published 23 January 2023)

Two-dimensional (2D) materials demonstrate fascinating thickness-dependent optical properties due to their van der Waals interaction and quantum confinement in the linear optical regime. However, the thickness-dependent nonlinear optical response is more complicated as virtual carriers (dipoles) and real carriers can be generated by below- and above-band-gap excitation, which calls for a more comprehensive understanding of these carriers in 2D materials. Herein, a direct band gap Bi_2S_3 is utilized to investigate the thickness-dependent nonlinear optical response by a terahertz (THz) emission spectroscopy. The results suggest that the THz emission intensity decreases with the increase of band gap energy under an 800-nm femtosecond laser excitation, which can be described by an empirical exponential equation. Under below-band-gap excitation, the optical rectification effect induced by instantaneous polarization (virtual carriers) dominates the THz emission mechanism in thin Bi_2S_3 films. In contrast, under above-band-gap excitation, real carriers are controlled by both resonant optical rectification and surface depletion electric field effects, resulting in shift and drift currents in thick Bi_2S_3 films. The contribution ratio of the shift and drift currents is $\sim 1:1$ at 45° oblique incidence. This competition between shift and drift currents results in the elliptically polarized THz wave generation, and the major axis orientation and ellipticity of the ellipse could be manipulated by changing the polarization of the pump light. In this paper, we imply the potential for designing tunable on-chip THz sources and nonlinear optoelectronic devices based on thickness-dependent 2D materials.

DOI: 10.1103/PhysRevB.107.035307

I. INTRODUCTION

Thickness is crucial for the fundamental investigation of intrinsic photon responses and optoelectronic properties of two-dimensional (2D) materials [1,2] in the linear optical regime. These excellent thickness-dependent optical properties of 2D materials are dominated by bound electron-hole pairs or excitons due to van der Waals interaction and quantum confinement [3], resulting in broad applications in active photonic and optoelectronic nanodevices [4]. Usually, the linear optical property of 2D materials is related to the optical band gap determined by the thickness of 2D materials. A typical example is a thickness-dependent transition from the direct to indirect band gap in MoS_2, which has the potential for next-generation tunable photonic devices [5]. Even for the semimetals such as graphene, the surface terahertz (THz) conductivity is also thickness dependent, which can be utilized for designing broadband THz antireflection layers [6]. However, the thickness-dependent nonlinear optical response becomes more complicated, attributing to the generation of intricate and dynamic photocarriers under below-band-gap (nonresonant) and above-band-gap (resonant) excitation. Some efforts have been made to advance the understanding of the thickness-dependent nonlinear optical response, such as revealing the transition of third-order nonlinear absorption induced by the tunable band gap [7] and the variable intensity of second-harmonic generation ascribing to the inversion symmetry broken [8]. Nonetheless, the evolution of photocarriers in thickness-dependent nonlinear optical processes is relatively less explored but significant for deepening the understanding of fundamental physics and boosting the development of compact optoelectronic devices based on 2D materials.

As a V-VI group transition metal chalcogenide, Bi_2S_3 possesses a tunable direct band gap from 1.3 to 1.8 eV [9], determined by the number of layers [10,11], which is attributed to the quantum confinement effect [12] and crystal size effect [13]. Although there is a tunable band gap with thickness in MoS_2, $MoSe_2$, $CsPb_2Br_5$, and WSe_2, these 2D semiconductor materials show a distinctive transition from an indirect band gap to a direct band gap [14–17]. This distinctive transition behavior complicates the physical process and hinders the exploration of nonlinear optical responses in 2D materials. Therefore, Bi_2S_3 with the thickness-dependent direct band gap becomes a more appropriate candidate for exploring the evolution of transient photocarriers in the nonlinear optical response.

*Corresponding author: yxzhou@nwu.edu.cn
†Corresponding author: xlxuphy@nwu.edu.cn

 ©2023 American Physical Society

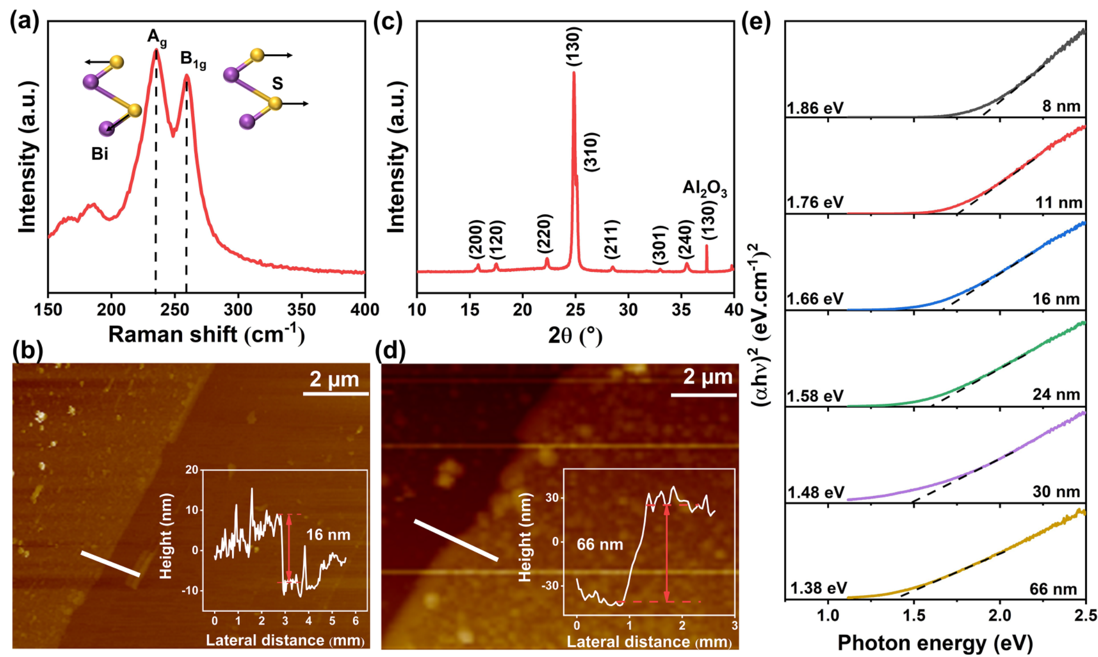

FIG. 1. Characterization of Bi_2S_3 films on sapphire substrates. (a) Raman spectroscopy with the excitation of 532 nm laser. (b) X-ray diffraction (XRD) spectrum of the Bi_2S_3 film. (c) and (d) Atomic force microscope (AFM) images of Bi_2S_3 films with different thicknesses. (e) Tauc plots of Bi_2S_3 films with different thicknesses measured by ultraviolet (UV)-visible absorption spectrum. The band gap energies are marked by the intersection of dotted lines and abscissa.

Unlike the common nonlinear optical research techniques such as Z-scan and second-harmonic generation, THz surface emission spectroscopy is a nondestructive tool to study the ultrafast nonlinear optical response in 2D semiconductor materials with both amplitude and phase information [18–20]. We have reported THz emission from bulk and monolayer $MoSe_2$, demonstrating the influence of limited thickness on a surface depletion electric field, which originates from real photocarriers under above-band-gap excitation [21]. However, the photocarrier evolution mechanism in thickness-dependent THz emission is still obscure. Moreover, THz surface emission spectroscopy has been verified to be an optical method to research the transverse and vertical components of the THz electric field, which can clarify the complex nonlinear optical responses and reconstruct the elliptically polarized THz wave in WSe_2 [22], $CrSiTe_3$ [23], $PdSe_2$ [24], and TaAs [25].

Herein, we investigate the THz emission properties of band-gap-tunable Bi_2S_3 films prepared by chemical vapor deposition (CVD) on sapphire substrates. The physical mechanisms of THz radiation from the thin (16 nm) and thick (66 nm) Bi_2S_3 films are found to be different by changing the azimuthal angle, polarization angle, power fluence, and incident angle of pump light. The THz radiation from the thin Bi_2S_3 film only results from the optical rectification effect. The THz radiation from the thick Bi_2S_3 film is induced by shift currents attributing to the resonant optical rectification effect and drift currents originating from the surface electric field (SEF) effect. Additionally, we can manipulate the elliptically polarized THz wave by tuning the polarization of pump light in the thick Bi_2S_3 film. In this paper, we suggest that the thickness-dependent Bi_2S_3 is an excellent candidate for designing tunable integrated THz emitters and optoelectronic devices.

II. EXPERIMENT

The Bi_2S_3 films with different thicknesses were prepared on sapphire (Al_2O_3) substrates via the CVD method. The detailed preparation process is described in the Supplemental Material [26] (see also Refs. [27–32] therein). The characterization of Bi_2S_3 films on sapphire substrates is shown in Fig. 1. Raman spectroscopy (Smart Raman confocal-micro-Raman module, Institute of semiconductors, Chinese Academy of Sciences) is utilized to analyze the vibration modes of crystal lattice under a 532-nm laser excitation. Figure 1(a) demonstrates two Raman vibration peaks at 189.09 and 235.49 cm^{-1}, which correspond to the A_g and B_{1g} modes of Bi_2S_3 [33], respectively. These phonon vibration modes are correlated to the transverse vibration and longitudinal vibration of sulfur atoms, respectively [34]. X-ray diffraction (XRD) spectroscopy (Bruker, D8 Advance), as shown in Fig. 1(b), is applied to verify the crystallographic structure of Bi_2S_3 films. There are seven distinct diffraction peaks corresponding to (200), (120), (220), (130), (310), (211), (300), and (240) crystal planes, suggesting that Bi_2S_3 is polycrystal [35]. The intensity of the diffraction peak located at the (130) crystal plane is the strongest, which manifests that the main crystal plane of Bi_2S_3 film is along the (130) direction. The XRD peaks also confirm the orthorhombic structure (D_{2h} point group) of Bi_2S_3 film without any impurity. The thicknesses of these Bi_2S_3 films are measured by an atomic force microscope (AFM, Bruker, Dimension Icon). Figures 1(c) and 1(d) show two samples with 16- and 66-nm thicknesses, respectively. Moreover, samples with thicknesses of 8, 11, 24, and 30 nm have also been prepared. Because the thickness of monolayer Bi_2S_3 film is ~1.117 nm [7], the layer numbers of the six samples are 7L,

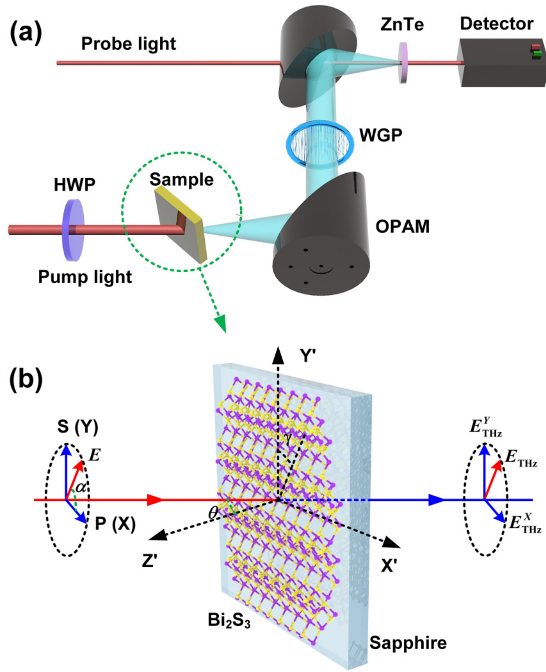

FIG. 2. (a) Schematic of THz emission spectroscopy with a transmission system. (b) Schematic diagram of the THz generation process from Bi_2S_3/sapphire sample excited by an 800 nm femtosecond laser.

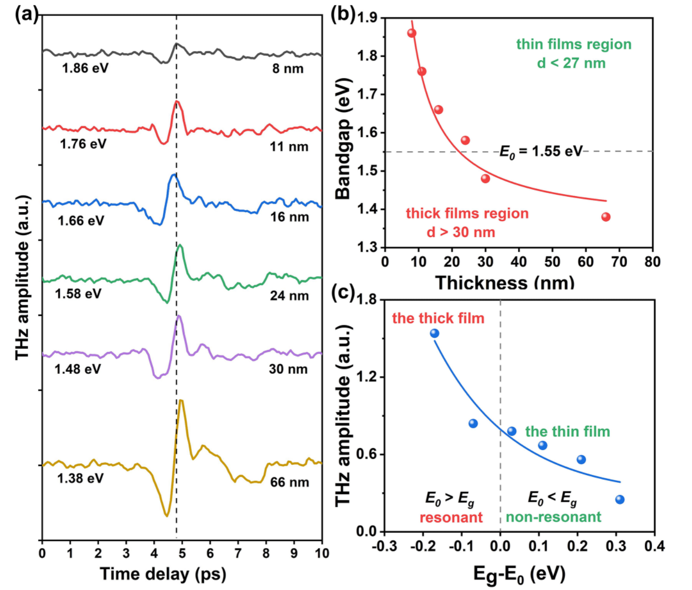

FIG. 3. (a) Time-domain signals of the Bi_2S_3 films with different thicknesses under p polarization light excitation. (b) Thickness-dependent band gap energies of Bi_2S_3 films. (c) E_0-E_g-dependent (THz) peak-to-valley amplitude. The band gap energies of the representative thick and thin Bi_2S_3 films are 1.38 and 1.86 eV, respectively.

10L, 14L, 22L, 27L, and 59L, respectively. The band gap energies (E_g) of these samples are given in Fig. 1(e). With the increase in the thickness, the band gap of Bi_2S_3 decreases from 1.86 to 1.38 eV. In addition, the absorption spectra of these samples are given in Fig. S1 in the Supplemental Material [26].

The THz signals emitted from Bi_2S_3 films are measured by THz surface emission spectroscopy [21], which is presented in Fig. 2(a). The femtosecond laser pulses are emitted from a Ti : sapphire laser, which possesses an 800-nm central wavelength, a pulse duration of 35 fs, and a 1-kHz repetition frequency. The pump beam excites the Bi_2S_3 film with an incident angle of 45°. The probe beam is used to detect the THz radiation by electric-optic sampling [36]. The half-wave plate (HWP) is applied to change the polarization direction of the linearly polarized light. The THz emission generated from the sample is gathered by two off-axis parabolic mirrors. Then it collinearly focuses onto a nonlinear crystal ⟨110⟩ ZnTe with the probe light together. The E^X_{THz} and E^Y_{THz} components of the THz electrical field can be detected by a single wire grid polarizer [37]. As shown in Fig. 2(b), XYZ is the laboratory coordinate system, and $X'Y'Z'$ presents the crystalline coordinate system. The α, θ, and γ represent the polarized angle of the pump light, the incidence angle of the pump light, and the azimuthal angle of the sample, respectively. The transverse and vertical components of the pump light are defined as E_X (corresponding to p polarization) and E_Y (corresponding to s polarization), respectively. The E^X_{THz} and E^Y_{THz} components correspond to the transverse and vertical components of the THz electric field.

III. RESULTS AND DISCUSSIONS

Under a p-polarized light excitation with a pump fluence of 0.56 mJ/cm^2, the total time-domain signals generated from Bi_2S_3 films with thicknesses increased from 8 to 66 nm are presented in Fig. 3(a). The amplitude of the THz electric field generated from Bi_2S_3 films enhances significantly with the increase of its thickness. This trend is different from the reported thickness-independent THz emission of Bi_2Te_3, which originates from the influence of a narrow band gap (∼0.5 eV) and topological surface states [38]. In addition, a tiny peak shift may result from the phase change due to the different thicknesses. The corresponding thickness-dependent frequency spectra are depicted in Fig. S2 (Supplemental Material [26]). With the increase of the material thicknesses, the bandwidths of frequency spectra keep almost the same. To explore the physical mechanism of the thickness-dependent THz emission from Bi_2S_3 films, the thickness-dependent band gap values are shown in Fig. 3(b). The experimental data can be well fitted by $E_g = E_g(\infty) + D_1/d$ [39], where E_g is the band gap of different thicknesses, $E_g(\infty)$ is the band gap of bulk materials, D_1 is the fitting parameter, and d is the film thickness. Furthermore, the THz peak-to-valley amplitude as a function of the band gap of the sample is presented in Fig. 3(c). It is obvious that the THz amplitudes present a reducing tendency with the increase of band gap, which can be described by an empirical exponential equation $E^{\text{total}}_{\text{THz}} \propto A_0 + A\exp[-\frac{(E_0-E_g)}{kT}]$. Here, $E^{\text{total}}_{\text{THz}}$ represents the integral THz amplitude, A_0 is the fitting parameters, A represents a pre-exponential factor, $E_0 - E_g$ represents the difference between the photon energy (E_0) and the material band gap (E_g), k is the Boltzmann constant, and T is the room temperature. Note that the thickness-dependent increasing tendency of THz emission differs from the reported decreased tendency of reduced

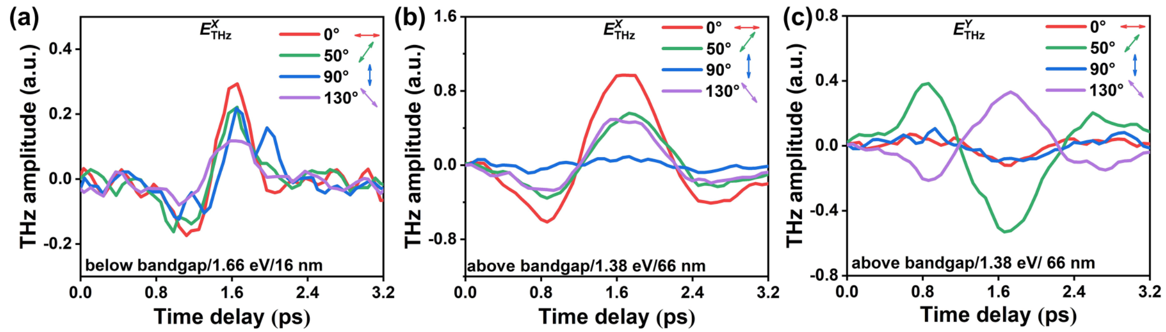

FIG. 4. (a) Time-domain signals of E^X_{THz} component from the thin Bi_2S_3 film (16 nm) with excitation polarization angles of 0°, 50°, 90°, and 130°. Time-domain signals of (b) E^X_{THz} and (c) E^Y_{THz} components from the thick Bi_2S_3 film (66 nm) with excitation polarization angles of 0°, 50°, 90°, and 130°.

graphene [40], indicating completely different mechanisms. Moreover, this empirical fitting reveals that the THz emission from Bi_2S_3 films is largely related to the energy difference between the excitation light and the band gap, which may be in connection with the conversion efficiency of virtual and real carriers. In addition, our femtosecond laser with the photon energy E_0 (1.55 eV) cuts across the band gaps of thin and thick Bi_2S_3 films, which affords an excellent platform to explore the evolution of photocarriers under below- and above-band-gap excitation. Therefore, we would like to investigate the THz emission mechanisms of two typical samples: the thin ($E_g = 1.66$ eV, 16 nm) and thick ($E_g = 1.38$ eV, 66 nm) Bi_2S_3 films.

Under below-band-gap excitation, only the E^X_{THz} component (without the E^Y_{THz} component) of THz emission is detected in the thin Bi_2S_3 film (as shown in Fig. S3 in the Supplemental Material [26]). According to the dipole radiation theory [32], this result suggests that the direction of the THz electric field is determined by the distribution of virtual carriers along the transverse orientation (Fig. 2). The corresponding time-domain signals of the E^X_{THz} component are presented in Fig. 4(a) with the excitation of polarized light. Under 0° polarized light excitation (corresponding to *p*-polarized light), the THz amplitude of the E^X_{THz} component is the largest, which is twice that of 130° polarized light excitation. The amplitude change suggests that THz emission is possibly governed by nonlinear optical effects due to their strong polarization direction dependence [41].

In comparison, under above-band-gap excitation, both E^X_{THz} and E^Y_{THz} components could be detected in the thick Bi_2S_3 film (66 nm), which suggests that the spatial distribution of real photocarriers is more intricate according to the dipole radiation theory. The corresponding time-domain signals of the E^X_{THz} and E^Y_{THz} components are shown in Figs. 4(b) and 4(c) under different polarization states of light excitation. Under the excitation of *p*-polarized light, the THz amplitude of the E^X_{THz} component is maximal, which is twice as large as that under 50° and 130° polarized light and eight times larger than that under 90° (corresponding to *s* polarized) polarized light excitation, as presented in Fig. 4(b). Compared with the E^X_{THz} component, the maximal amplitude of the E^Y_{THz} component is presented at 50° polarized light excitation, which is about five times larger than that under the excitation of *p*- and *s*-polarized light, as shown in Fig. 4(c). These results indicate that complicated and dynamic real photocarriers could result in different THz radiation mechanisms in the thick Bi_2S_3 film. Moreover, the huge THz amplitude difference and opposite polarity of the E^Y_{THz} component also suggest the existence of a nonlinear optical response dominating the THz radiation [42]. Furthermore, the results are like the reported phenomenon in WS_2 with THz radiation induced by a strong surface built-in field effect under above-band-gap excitation [43]. These results suggest that at least two physical mechanisms are responsible for the E^X_{THz} and E^Y_{THz} components in the thick Bi_2S_3 film.

To clarify the physical mechanisms in the thin (16 nm) and thick (66 nm) Bi_2S_3 films, the pump fluence, azimuthal angle, and polarization angle dependencies on the THz amplitude are investigated. First, under below-band-gap excitation, the THz amplitude of the E^X_{THz} component in the thin Bi_2S_3 film exhibits a linear dependence of pump fluence under the *p*-polarized pump beam with an incidence angle of 45°, as presented in Fig. 5(a). This suggests that THz emission in the thin Bi_2S_3 film is mainly ascribed to second-order nonlinear optical effects induced by virtual photocarriers [44]. It can be well fitted with $E^X_{\mathrm{THz}} \propto \chi^{(2)}|E(t)|^2 \propto I_{\mathrm{pump}}$ [21], where $\chi^{(2)}$ is the second-order nonlinear susceptibility, $E(t)$ is the electric field of pump light, and I_{pump} is the pump intensity. Note that second-order nonlinear optical effects are forbidden in centrosymmetric crystals; however, inversion symmetry breaking usually happens at the surface of transition metal chalcogenides due to structure reconstruction or lattice defects [28,29]. In comparison, under above-band-gap excitation, the THz amplitude of the E^X_{THz} component dependence on pump fluence shows a saturation trend from the thick Bi_2S_3 film, as shown in Fig. 5(b). This trend mainly results from the photon-generated real carriers accelerated by the SEF, which could screen the THz wave when the pump fluence rises [45]. This result can be fitted well with $E^X_{\mathrm{THz}} \propto D_3F/(F + F_{\mathrm{sat}})$ [46], as shown in Fig. 5(b). Here, D_3 is a constant factor, and F_{sat} is saturation pump fluence (0.85 mJ/cm^2). On the other hand, as shown in Fig. 5(c), the THz amplitude of the E^Y_{THz} component presents a linear dependence of pump fluence in the thick Bi_2S_3 film. It suggests that the E^Y_{THz} component mainly originates from the second-order nonlinear effects induced by real photocarriers. The THz amplitude dependent on pump fluence under below- and above-band-gap excitation shows distinctive physical mechanisms

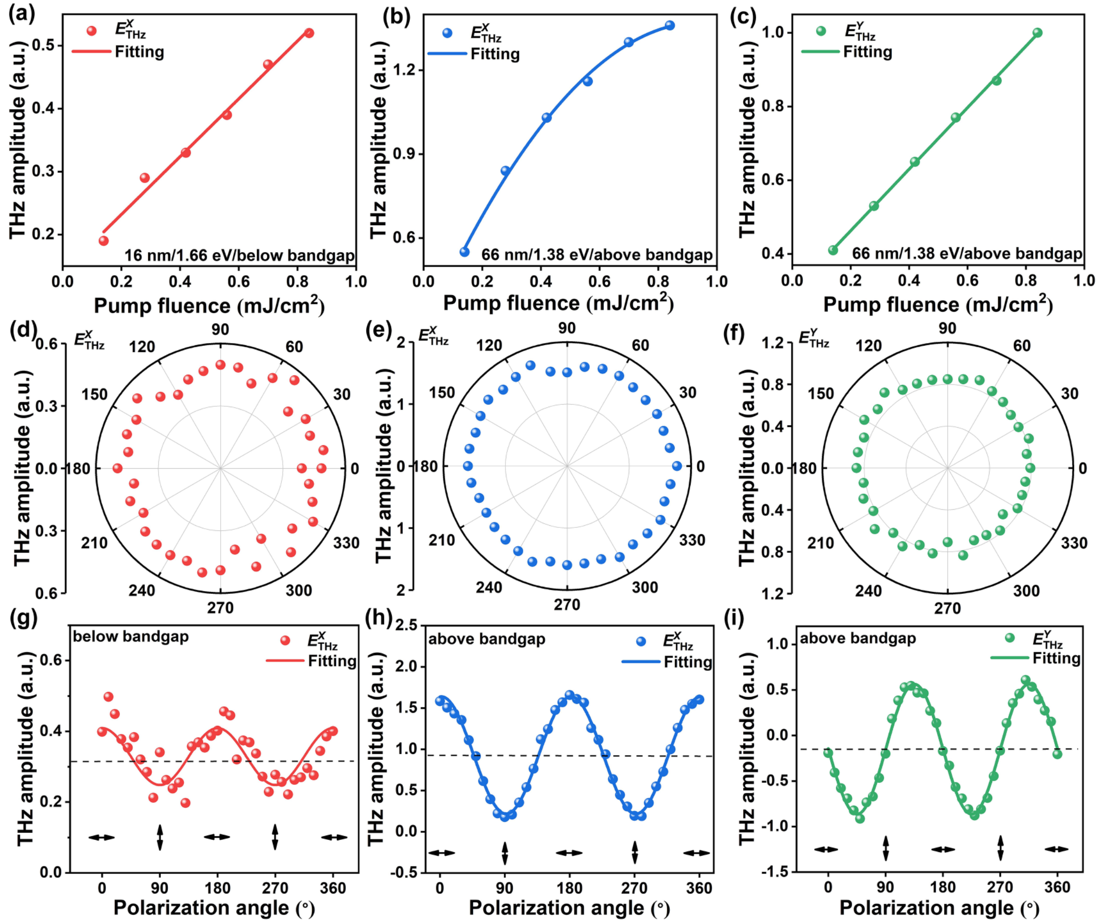

FIG. 5. Pump-fluence-dependent (a) E^X_{THz} component of the thin (16 nm) Bi_2S_3 film, (b) E^X_{THz} component, and (c) E^Y_{THz} component of the thick (66 nm) Bi_2S_3 film. Azimuthal-angle-dependent (d) E^X_{THz} component of the thin Bi_2S_3 film, (e) E^X_{THz} component, and (f) E^Y_{THz} component of the thick Bi_2S_3 film. Polarization-angle-dependent (g) E^X_{THz} component of the thin Bi_2S_3 film, (h) E^X_{THz} component, and (i) E^Y_{THz} component of the thick Bi_2S_3 film.

dominating the THz radiation due to dynamic virtual and real photocarriers.

We further investigate the azimuthal angle-dependent THz amplitude, which is isotropic in both the thin (16 nm) and thick (66 nm) Bi_2S_3 films, as illustrated in Figs. 5(d)–5(f). It suggests that the THz radiation induced by virtual and real photocarriers is averaged along each crystal direction in our Bi_2S_3 films. These experimental results are consistent with the polycrystal structure, as demonstrated in Fig. 1(b). The THz radiation dependent on the azimuthal angle isotropic is also reported in WS_2, which originates from nonlinear optical coefficients without obvious azimuthal dependence [41]. In contrast, this isotropic dependence is different from THz emission from thermoelectric semimetal Gd_3As_2, which is relevant to the anisotropic in-plane Seebeck current [47]. The azimuthal-angle-insensitive property of polycrystal Bi_2S_3 films is beneficial to develop advanced THz emitters and optoelectronic devices.

Moreover, the polarization angle dependence of the THz amplitude is investigated by tuning the HWP from 0° to 360° with a fixed azimuthal angle. Under below-band-gap excitation, the E^X_{THz} component of the THz electric field from the thin (16 nm) Bi_2S_3 film presents a periodic change combined with an upward offset, as shown in Fig. 5(g). This result further proves the contribution of the second-order nonlinear effect induced by virtual carriers. Under above-band-gap excitation, the THz amplitudes of the E^X_{THz} and E^Y_{THz} components from the thick (66 nm) Bi_2S_3 film exhibit a twofold rotational symmetry dependent on the polarization angle, as shown in Figs. 5(h) and 5(i). For the E^X_{THz} component, there is a large upward offset from the average THz amplitude, as shown in Fig. 5(h). This offset may result from a background current motivated by real carriers [42]. Unlike the E^X_{THz} component, a tiny downward offset of the E^Y_{THz} component is presented in Fig. 5(i), which suggests that the background current almost vanishes.

In the following part, theoretical deduction and analysis are performed for a deep understanding of the thickness-dependent nonlinear optical processes. The THz electric field excited by the femtosecond laser originates from the transient dielectric polarization or photocurrents in nonmagnetic materials, which can be expressed as $E^X_{\mathrm{THz}} \propto \frac{\partial^2 P}{\partial t^2} + \frac{\partial J}{\partial t}$ [48]. Here, P is the instantaneous nonlinear dielectric polarization, and J is the transient photocurrent density. Under below-band-gap excitation, due to the linear pump fluence dependence, THz emission from the thin Bi_2S_3 film (16 nm) is attributed to the optical rectification effect originating from instantaneous nonlinear polarization of dipoles [49], which can be

described as

$$P_i^{(2)} = \chi_{ijk}^{(2)}(0, \omega, -\omega)E_j(\omega)E_k^*(\omega), \quad (1)$$

where $\chi_{ijk}^{(2)}$ is the second-order nonlinear susceptibility, representing the rectification components and reflecting the displacement of virtual carriers. Due to the inversion symmetry breaking, the point group of Bi_2S_3 at the surface could be transformed from D_{2h} to C_{2v}, whose second-order nonlinear susceptibility is given as Eq. (S1) in the Supplemental Material [26]. The projection of electrical vectors in crystalline coordinate $X'Y'Z'$ [Fig. 2(a)] can be expressed by the Jones matrix in Eq. (S2) in the Supplemental Material [26]. Then based on dipole radiation [31], the optical-rectification-effect-induced THz emission of the E_{THz}^X component can be expressed as

$$E_{\mathrm{THz-OR}}^X \propto -P_{Z'} \cos\theta_{\mathrm{THz}} + P_{X'} \sin\theta_{\mathrm{THz}}, \quad (2)$$

where θ_{THz} is the refraction angle of the THz waves that can be obtained by $n_{\mathrm{air}} \sin\theta_{\mathrm{in}} = n_{\mathrm{THz}} \sin\theta_{\mathrm{THz}}$. Hence, the polarization-angle-dependent $E_{\mathrm{THz-OR}}^X$ component can be calculated by

$$E_{\mathrm{THz-OR}}^X \propto A_1 \cos^2(\alpha) + B_1 \sin^2(\alpha) + C_1, \quad (3)$$

where A_1, B_1, and C_1 are constants relating to the second-order nonlinear susceptibility tensors, which can be described as

$$\begin{aligned} A_1 &= E_0^2\big[\chi_{XZX}^{(2)} \sin(2\theta) cos(\theta_{\mathrm{THz}}) \\ &\quad - \chi_{ZXX}^{(2)} \cos^2(\theta) \sin(\theta_{\mathrm{THz}}) - \chi_{ZZZ}^{(2)} \sin^2(\theta) \sin(\theta_{\mathrm{THz}})\big], \\ B_1 &= -E_0^2 \chi_{ZYY}^{(2)} \sin(\theta_{\mathrm{THz}}), \\ C_1 &= \chi_{YYZ}^{(2)} \sin(\theta_{\mathrm{THz}}) - \chi_{ZZY}^{(2)} \cos(\theta_{\mathrm{THz}}). \end{aligned} \quad (4)$$

The experimental data in Fig. 5(g) can be well fitted with Eq. (3). The upward offset in Fig. 5(g) is related to the constant term of second-order nonlinear susceptibility tensors rather than background currents induced by real photocarriers [43]. The result reveals that the THz radiation from the thin Bi_2S_3 film (16 nm) under below-band-gap excitation is dominated by the optical rectification effect driven by instantaneous polarization (virtual carriers).

However, under above-band-gap excitation, the physical mechanisms of THz emission from the thick Bi_2S_3 film (66 nm) are complicated because real photocarriers can give rise to dynamic transient photocurrents in various ways. Generally, the transient photocurrents excited by linear polarized light can be divided by

$$J_{\mathrm{real}} = J_{\mathrm{drift}} + J_{\mathrm{diffusion}} + J_{\mathrm{shift}} + J_{\mathrm{photondrag}}, \quad (5)$$

where J_{drift}, $J_{\mathrm{diffusion}}$, J_{shift}, and $J_{\mathrm{photondrag}}$ are drift, diffusion, shift, and photon-drag currents, respectively. The saturation trend in Fig. 5(b) suggests the possible existence of diffusion current ($J_{\mathrm{diffusion}}$) driven from the photo-Dember effect and the drift current (J_{drift}) resulting from the surface depletion electric field effect [50]. The photo-Dember effect originates from the huge difference in mobilities between electrons and holes [46], such as in the narrow band gap semiconductor InAs (33 000 $\mathrm{cm^2\,V^{-1}\,S^{-1}}$ for electrons and 460 $\mathrm{cm^2\,V^{-1}\,S^{-1}}$ for holes) [51]. Here, the mobility of electrons (1100 $\mathrm{cm^2\,V^{-1}\,S^{-1}}$) is five times larger than that of holes (200 $\mathrm{cm^2\,V^{-1}\,S^{-1}}$) in Bi_2S_3 films [52], so the possible weak photo-Dember effect can be neglected in the thick Bi_2S_3 film. Therefore, the J_{drift} resulting from the surface depletion electric field effect makes a significant contribution to the E_{THz}^X component of THz emission. As the second-order nonlinear optical process, the resonant optical rectification and the photon-drag effect could generate transient nonlinear photocurrents of the shift current (J_{shift}) [53] and the photon-drag current ($J_{\mathrm{photondrag}}$), respectively. Here, the photon-drag effect has been reported in graphene [54] and heavy metal-doped semiconductors [55] with large carrier densities and high carrier mobilities [56]. Moreover, when the photon-drag effect governs the THz generation process, the polarity reversal of the THz wave could be found by reversing the incident direction [54]. In our experiment, this reversal polarity phenomenon has not been observed in the thick Bi_2S_3 film, as illustrated in Figs. S4(a) and S4(b) in the Supplemental Material [26]. Hence, the photon-drag effect could be excluded in the thick (66 nm) Bi_2S_3 film. As a result, the resonant optical rectification effect should contribute to the E_{THz}^X component, which is consistent with the polarization-sensitive THz amplitude in Fig. 5(h) [57]. Based on the above discussions, it is unambiguous that both J_{drift} induced by the surface depletion electric field effect and J_{shift} resulting from the resonant optical rectification effect dominate the E_{THz}^X component of THz emission under above-band-gap excitation. Additionally, according to the linear pump fluence dependence in Fig. 5(c) and the tiny downward offset in Fig. 5(i), we confirm that only J_{shift} resulting from the resonant optical rectification effect makes a significant contribution to the E_{THz}^Y component under above-band-gap excitation.

To further explore the effect of transient nonlinear photocurrents on THz emission of E_{THz}^X and E_{THz}^Y components in the thick Bi_2S_3 film, the instantaneous second-order nonlinear photocurrent J_{shift} is expressed as [58,59]

$$J_\lambda = \sigma_{\lambda\mu\nu}^{(2)} \frac{E_\mu E_\nu^* + E_\nu E_\mu^*}{2}, \quad (6)$$

where $\sigma_{\lambda\mu\nu}^{(2)}$ is the second-order nonlinear conductivity, which can be expressed as Eq. (S6) in the Supplemental Material [26]. The $\sigma_{\lambda\mu\nu}^{(2)}$ term arises from the spatial shift of the center of photogenerated charges and leads to the shift current under above-band-gap excitation. With a dipole radiation model [31], the resonant optical-rectification-effect-induced THz components in the laboratory coordinate [as shown in Fig. 2(b)] can be expressed as

$$E_{\mathrm{THz-ROR}}^X \propto t_p\left(\frac{\partial J_{\mathrm{shift}}^{X'}}{\partial t} \cos\theta_{\mathrm{THz}} + \frac{\partial J_{\mathrm{shift}}^{Z'}}{\partial t} \sin\theta_{\mathrm{THz}}\right), \quad (7)$$

$$E_{\mathrm{THz-ROR}}^Y \propto t_s \frac{\partial J_{\mathrm{shift}}^{Y'}}{\partial t}, \quad (8)$$

where t_p and t_s are transmission Fresnel coefficients at the air-sample interface for p and s polarization, respectively. Therefore, the THz emission components varying with the polarization angle of pump light can be

deduced by

$$E^X_{\text{THz-ROR}} \propto A_2\cos^2(\alpha) + B_2\sin^2(\alpha) + C_2, \quad (9)$$

$$E^Y_{\text{THz-ROR}} \propto A_3 \sin(2\alpha), \quad (10)$$

where A_2, B_2, C_2, and A_3 are related to the second-order nonlinear photoconductivity coefficients, which are given as the following:

$$A_2 = E_0^2\big[\sigma^{(2)}_{XZX}\sin(2\theta)\cos(\theta_{\text{THz}}) - \sigma^{(2)}_{ZXX}\cos^2(\theta)\sin(\theta_{\text{THz}}) - \sigma^{(2)}_{ZXX}\sin^2(\theta)\sin(\theta_{\text{THz}})\big],$$
$$B_2 = -E_0^2\sigma^{(2)}_{ZYY}\sin(\theta_{\text{THz}}),$$
$$C_2 = \sigma^{(2)}_{YYZ}\sin(\theta_{\text{THz}}) - \sigma^{(2)}_{ZZY}\cos(\theta_{\text{THz}}),$$
$$A_3 = E_0^2\sigma^{(2)}_{YYZ}\sin(\theta_{\text{THz}}). \quad (11)$$

The experimental data in Figs. 5(h) and 5(i) can be well fitted with Eqs. (9) and (10). It is worth noting that Eqs. (3) and (9) have the same functional form, while they are theoretically different considering the microscopic meanings of A_1–C_1 in Eq. (4) and A_2–C_2 in Eq. (11). However, from an experimental viewpoint, the optical rectification and resonant optical rectification effects cannot be distinguished only from the polarization-angle-dependent twofold rational symmetry of E^X_{THz}. Here, these two mechanisms can be confirmed by the different excitation conditions, in which the excitation photon energy (1.55 eV) is below and above band gap for the thin (1.66 eV) and thick (1.38 eV) Bi_2S_3 films, respectively. Moreover, the different microscopic processes dominated by instantaneous polarization and transient photocurrent can also be supported by the linear and saturable dependence of the pump fluence [Figs. 5(a) and 5(b)] because the saturation of the THz amplitude is induced by real carriers that can screen the THz wave at the high pump fluence region.

The large offset in Fig. 5(h) mainly results from the background current induced by the surface depletion electric field and the constant term relating to the second-order nonlinear conductivity tensors [42]. The upward offset in Fig. 5(g) is smaller than that in Fig. 5(h), which is attributed to the nonexistent real photocarriers in the thin Bi_2S_3 film under below-band-gap excitation. Note that the polarity reversal of the E^X_{THz} component is not observed at different polarization angles, which can be attributed to the large influence of the polarization-insensitive background current J_{drift} on the polarization-sensitive nonlinear current J_{shift}. Additionally, the contribution proportion of J_{shift} in the E^X_{THz} component is ~44%, calculated by $(E_{\max} - E_{\min})/2E_{\max}$, so the ratio of J_{drift} to J_{shift} is close to 1:1 with an incidence angle of 45°. Unlike the E^X_{THz} component, the downward offset of the E^Y_{THz} component is slight, and the polarity reversal of the THz waveform occurs by varying the polarization angle of pump light periodicity, as shown in Fig. 5(i). This phenomenon implies that the E^Y_{THz} component is primarily dominated by the resonant optical rectification effect. The contribution of J_{shift} is ~88% for the E^Y_{THz} component.

Further, we summarize the photocarrier evolution mechanisms in thickness-dependent nonlinear optical processes for the THz radiation from Bi_2S_3 films. Under below-band-gap

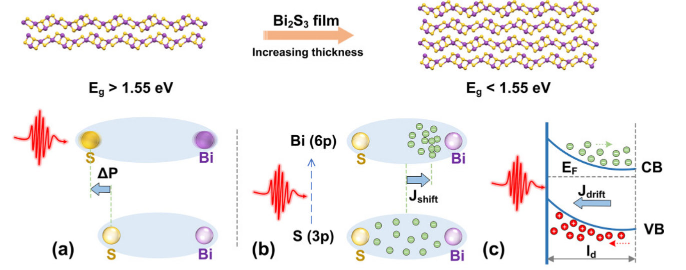

FIG. 6. (a) Schematic of the optical rectification effect under below-band-gap excitation in thin Bi_2S_3 films. Schematic of (b) the resonant optical rectification effect and (c) the surface depletion electric field effect under above-band-gap excitation in thick Bi_2S_3 films.

excitation, the optical rectification effect dominates the THz radiation from the thin Bi_2S_3 film (16 nm), as shown in Fig. 6(a). Under the excitation of an 800-nm femtosecond laser, the electric field oscillation of the electromagnetic wave induces oscillating dipoles (virtual electron-hole pairs), of which the position variations result in time-dependent nonlinear polarization ΔP and further generate THz emission [60]. Under above-band-gap excitation, real photocarriers are generated and form transient photocurrents, including J_{shift} and J_{drift} in the thick Bi_2S_3 film (66 nm). The J_{shift} induced by the resonant optical rectification effect in thick Bi_2S_3 film is presented in Fig. 6(b). Since the conduction band (CB) minimum is dominated by Bi 6p states and the valence band (VB) maximum is occupied by S 3p states [61], the photocarriers will shift from S atoms to Bi atoms after the resonant excitation. Such spatial charge center movements from the VB to the CB would result in an instantaneous nonlinear photocurrent J_{shift} and give rise to the THz wave output [62]. Meanwhile, the schematic of the J_{drift} induced by the surface depletion field is presented in Fig. 6(c). Under above-band-gap excitation, the Fermi level difference between the surface and bulk states induces energy band bending, which forms a surface depletion field. In this built-in electric field, photogenerated electrons and holes are separated and induce J_{drift}, which will generate THz waves. Here, the SEF can be calculated by $E_{\text{SEF}} = eN_D l_d/\varepsilon_0\varepsilon_r$ [63], where the vacuum permittivity ε_0 is 8.85×10^{-12} F/m, $\varepsilon_r = 2.214$ is the relative dielectric constant of Bi_2S_3 [64], $N_D = 3.51 \times 10^{17}$ cm^{-3} is the carrier concentration [65], and l_d is the width of the surface depletion layer. The l_d can be expressed as $l_d = \sqrt{(2\varepsilon_0\varepsilon_r/eN_D)[V_D - (kT/e)]}$, where the built-in potential V_D is 0.39 V [66], and $kT/e = 0.026$ is the thermal energy. As a result, l_d is calculated to be ~156 nm, and E_{SEF} is ~4.64×10^4 V/m. The width of the surface depletion layer l_d is larger than the thickness of the thick Bi_2S_3 film (66 nm). Additionally, the carrier concentration N_D and built-in potential V_D increase with the increase in thickness of the Bi_2S_3 film [67]. Therefore, within the penetration depth, we infer that the surface depletion electric field E_{SEF} would be enhanced with the increase of Bi_2S_3 film thickness.

According to the THz emission mechanism under above-band-gap excitation, the competition between J_{drift} and J_{shift} in the thick Bi_2S_3 film (66 nm) results in the differences in amplitude and phase between the E^X_{THz} and E^Y_{THz}

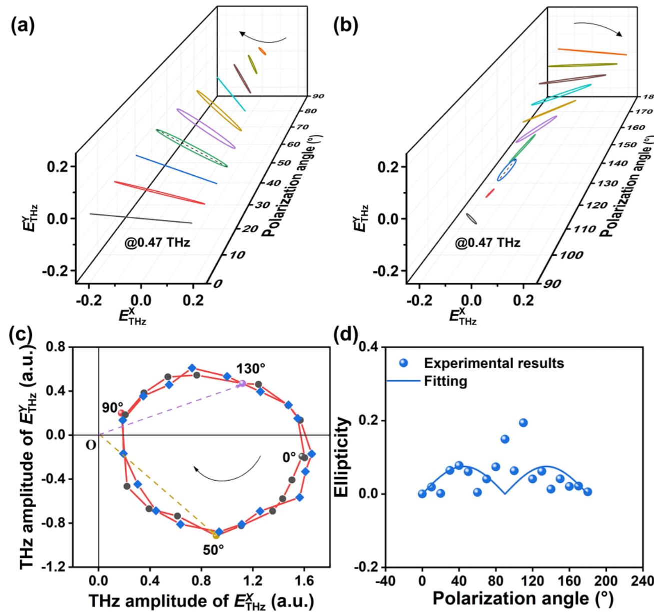

FIG. 7. The reconstruction of (THz) polarization ellipse based on E^X_{THz} and E^Y_{THz} components of the thick (66 nm) Bi_2S_3 film at (a) 0°–90° and (b) 90°–180° polarization angles at the 0.47 THz central frequency. (c) Polar plot of the E^X_{THz} and E^Y_{THz} amplitude of the thick Bi_2S_3 film as changing the polarization angle from 0° to 180° (black circular dots) and 190° to 360° (blue square dots). The solid red line constitutes an ellipse, which represents the two round rotation trajectories of the shift current. (d) The polarization angle dependence of the THz polarization ellipticity at 0.47 THz.

components at different polarization angles of pump light. In turn, it is possible to reconstruct elliptically polarized THz waves from the thick Bi_2S_3 film using the interplay of J_{shift} and J_{drift}. Herein, we have reconstructed the THz polarization ellipses by $E(\omega) = E^X_{THz}\hat{e}_x + E^Y_{THz}\hat{e}_y$ at the central frequency of 0.47 THz, as shown in Figs. 7(a) and 7(b). The elliptically polarized THz wave is periodically tuned by varying the polarization angle. Furthermore, the principal axis of the THz polarized ellipse has a clockwise rotation by changing the polarization angle from 0° to 180°. This is mainly due to the different contribution ratios of J_{shift} and J_{drift} for E^X_{THz} and E^Y_{THz} components at different polarization angles since J_{drift} is independent of the polarization angle. As shown in Fig. 7(c), the polar plot of the amplitude of E^X_{THz} and E^Y_{THz} components [data from Figs. 5(h) and 5(i)] represents the shift current flowing at different polarization angles. Taking the HWP of 50° and 130° as examples, E^Y_{THz} presents opposite THz waveforms embodied by the positive and negative values, as indicated by the purple and orange dashed lines, respectively. This result suggests that the $J_{Y'}$ component of the J_{shift} flows along opposite directions at $\alpha = 50°$ and 130°. After rotating α from 0° to 180°, J_{shift} also has a clockwise rotation and repeats the same rotation as α increasing from 180° to 360°, which verifies the J_{shift} dominance on the principal axis rotation of the THz polarization ellipse. Based on the E^X_{THz} and E^Y_{THz} components, we can obtain the ellipticity of the THz wave by $\chi = \frac{E^Y_{THz}}{E^X_{THz}} \exp(i|\delta_y - \delta_x|)$ [68], as shown in Fig. 7(d). When changing α from 0° to 180°, the ellipticity χ of the elliptically polarized THz waves is tuned from 0 to 0.2. This result clarifies the interplay mechanism between the photocurrents in thick Bi_2S_3 film and provides a promising way to control the polarized THz emission, which is promising for designing advanced THz components.

IV. CONCLUSIONS

The thickness-dependent THz radiation from Bi_2S_3 films is investigated by THz surface emission spectroscopy. With the Bi_2S_3 film thickness increasing from 16 to 66 nm, its band gap energy decreases from 1.86 to 1.38 eV, presenting a thickness-dependent nonlinear optical response. Under below-band-gap excitation, the optical rectification effect induced by instantaneous polarization (virtual carriers) significantly dominates THz emission from the thin Bi_2S_3 film (16 nm). Under above-band-gap excitation, the E^X_{THz} component of THz radiation from the thick Bi_2S_3 film (66 nm) is demonstrated to result from the shift current driven by the resonant optical rectification effect with a contribution of 44% and the drift current resulting from the surface depletion electric field effect. In comparison, the E^Y_{THz} component mainly originates from the shift current motivated by the resonant optical rectification, which has ∼88% contribution to the THz radiation. Furthermore, the competition between the shift and drift currents induces a tunable elliptically polarized THz wave under above-band-gap excitation. These results reveal the evolution mechanisms of nonresonant and resonant nonlinear optical processes in Bi_2S_3 films with different thicknesses and pave the way forward to develop tunable THz devices based on 2D materials.

ACKNOWLEDGMENTS

This paper was supported by National Natural Science Foundation of China (Grants No. 11974279, No. 12074311, No. 12004310, No. 12261141662, and No. 12104368), Natural Science Foundation of Shaanxi Province (Grant No. 2020JQ-567), and Natural Science Foundation of Education Department of Shaanxi Province (Grant No. 21JK0917).

[1] K. Synnatschke, P. A. Cieslik, A. Harvey, A. Castellanos-Gomez, T. Tian, C.-J. Shih, A. Chernikov, E. J. G. Santos, J. N. Coleman, and C. Backes, Chem. Mater. **31**, 10049 (2019).

[2] L.-Y. Pan, Y.-F. Ding, Z.-L. Yu, Q. Wan, B. Liu, and M. Q. Cai, J. Power Sources **451**, 227732 (2020).

[3] G. Wang, A. Chernikov, M. M. Glazov, T. F. Heinz, X. Marie, T. Amand, and B. Urbaszek, Rev. Mod. Phys. **90**, 021001 (2018).

[4] J. W. You, S. R. Bongu, Q. Bao, and N. C. Panoiu, Nanophotonics **8**, 63 (2019).

[5] S. Mukherjee, R. Maiti, A. Midya, S. Das, and S. K. Ray, ACS Photonics **2**, 760 (2015).

[6] Y. Zhou, X. Xu, F. Hu, X. Zheng, W. Li, P. Zhao, J. Bai, and Z. Ren, Appl. Phys. Lett. **104**, 051106 (2014).
[7] C. Lu, M. Luo, Y. Ge, Y. Huang, Q. Zhao, Y. Zhou, and X. Xu, ACS Appl. Mater. Interfaces **14**, 2390 (2022).
[8] W. Jie, X. Chen, D. Li, L. Xie, Y. Y. Hui, S. P. Lau, X. Cui, and J. Hao, Angew. Chem. **127**, 1201 (2015).
[9] M. Bouachri, H. El Farri, M. Beraich, M. Taibi, K. Nouneh, and M. Fahoume, Materialia **20**, 101242 (2021).
[10] X. Meng and Z. Zhang, J. Mol. Catal. A: Chem. **423**, 533 (2016).
[11] Y. Zhao, D. Gao, J. Ni, L. Gao, J. Yang, and Y. Li, Nano Res. **7**, 765 (2014).
[12] M. Aresti, M. Saba, R. Piras, D. Marongiu, G. Mula, F. Quochi, A. Mura, C. Cannas, M. Mureddu, A. Ardu *et al.*, Adv. Funct. Mater. **24**, 3341 (2014).
[13] E. Zahedi, Superlattices Microstruct. **81**, 49 (2015).
[14] K. F. Mak, C. Lee, J. Hone, J. Shan, and T. F. Heinz, Phys. Rev. Lett. **105**, 136805 (2010).
[15] Y. Zhang, T.-R. Chang, B. Zhou, Y.-T. Cui, H. Yan, Z. Liu, F. Schmitt, J. Lee, R. Moore, Y. Chen *et al.*, Nat. Nanotechnol. **9**, 111 (2014).
[16] P. Acharyya, P. Pal, P. K. Samanta, A. Sarkar, S. K. Pati, and K. Biswas, Nanoscale **11**, 4001 (2019).
[17] S. B. Desai, G. Seol, J. S. Kang, H. Fang, C. Battaglia, R. Kapadia, J. W. Ager, J. Guo, and A. Javey, Nano Lett. **14**, 4592 (2014).
[18] Y. H. Tao, A. J. Fitzgerald, and V. P. Wallace, Sensors **20**, 712 (2020).
[19] Y. Huang, Z. Yao, C. He, L. Zhu, L. Zhang, J. Bai, and X. Xu, J. Phys.: Condens. Matter **31**, 153001 (2019).
[20] W. Du, Y. Huang, Y. Zhou, and X. Xu, J. Phys. D: Appl. Phys. **55**, 223002 (2022).
[21] Z. Fan, M. Xu, Y. Huang, Z. Lei, L. Zheng, Z. Zhang, W. Zhao, Y. Zhou, X. Wang, X. Xu *et al.*, ACS Appl. Mater. Interfaces **12**, 48161 (2020).
[22] J. Chang, H. Wang, Z. Lei, W. Du, Y. Huang, Y. Zhou, L. Zhu, and X. Xu, J. Phys. Chem. Lett. **12**, 10068 (2021).
[23] P. Suo, W. Xia, W. Zhang, X. Zhu, J. Fu, X. Lin, Z. Jin, W. Liu, Y. Guo, and G. Ma, Laser Photonics Rev. **14**, 2000025 (2020).
[24] H. Wang, J. Chang, Y. Huang, Z. Lei, W. Du, Y. Zhou, Y. E, and X. Xu, ACS Appl. Mater. Interfaces **13**, 54543 (2021).
[25] Y. Gao, S. Kaushik, E. J. Philip, Z. Li, Y. Qin, Y. P. Liu, W. L. Zhang, Y. L. Su, X. Chen, H. Weng *et al.*, Nat. Commun. **11**, 720 (2020).
[26] See Supplemental Material at http://link.aps.org/supplemental/10.1103/PhysRevB.107.035307 for more experimental results.
[27] M. Qi, Z. Ren, Y. Jiao, Y. Zhou, X. Xu, W. Li, J. Li, X. Zheng, and J. Bai, J. Phys. Chem. C **117**, 14348 (2013).
[28] Y. Li, Y. Rao, K. F. Mak, Y. You, S. Wang, C. R. Dean, and T. F. Heinz, Nano Lett. **13**, 3329 (2013).
[29] R. Milkus and A. Zaccone, Phys. Rev. B **93**, 094204 (2016).
[30] S. L. Lawton, C. J. Fuhrmeister, R. G. Haas, C. S. Jarman, and F. G. Lohmeyer, Inorg. Chem. **13**, 135 (1974).
[31] M. B. Johnston, D. M. Whittaker, A. Corchia, A. G. Davies, and E. H. Linfield, J. Appl. Phys. **91**, 2104 (2002).
[32] S. Matsuura, M. Tani, and K. Sakai, Appl. Phys. Lett. **70**, 559 (1997).
[33] F. Lu, R. Li, Y. Li, N. Huo, J. Yang, Y. Li, B. Li, S. Yang, Z. Wei, and J. Li, ChemPhysChem **16**, 99 (2015).
[34] R. M. Clark, J. C. Kotsakidis, B. Weber, K. J. Berean, B. J. Carey, M. R. Field, H. Khan, J. Z. Ou, T. Ahmed, C. J. Harrison *et al.*, Chem. Mater. **28**, 8942 (2016).
[35] Z. Zhang, W. Wang, L. Wang, and S. Sun, ACS Appl. Mater. Interfaces **4**, 593 (2012).
[36] A. Nahata, A. S. Weling, and T. F. Heinz, Appl. Phys. Lett. **69**, 2321 (1996).
[37] Y. Zhang, Y. Chen, S. Xu, H. Lian, M. Wang, W. Liu, S. L. Chin, and G. Mu, Opt. Lett. **34**, 2841 (2009).
[38] Z. Fang, H. Wang, X. Wu, S. Shan, C. Wang, H. Zhao, C. Xia, T. Nie, J. Miao, C. Zhang *et al.*, Appl. Phys. Lett. **115**, 191102 (2019).
[39] X. Yao, Y. Wang, X. Lang, Y. Zhu, and Q. Jiang, Physica E **109**, 11 (2019).
[40] H. Wang, Y. Zhou, Z. Yao, L. Zhu, Y. Huang, X. Xu, and Z. Ren, Carbon **134**, 439 (2018).
[41] L. Zhang, Y. Huang, Q. Zhao, L. Zhu, Z. Yao, Y. Zhou, W. Du, and X. Xu, Phys. Rev. B **96**, 155202 (2017).
[42] Y. Huang, L. Zhu, Q. Zhao, Y. Guo, Z. Ren, J. Bai, and X. Xu, ACS Appl. Mater. Interfaces **9**, 4956 (2017).
[43] L. Zhang, Y. Huang, L. Zhu, Z. Yao, Q. Zhao, W. Du, Y. He, and X. Xu, Adv. Opt. Mater. **7**, 1801314 (2019).
[44] C. Gollner, M. Shalaby, C. Brodeur, I. Astrauskas, R. Jutas, E. Constable, L. Bergen, A. Baltuška, and A. Pugžlys, APL Photonics **6**, 046105 (2021).
[45] B. B. Hu, X. C. Zhang, and D. H. Auston, Phys. Rev. Lett. **67**, 2709 (1991).
[46] M. Reid and R. Fedosejevs, Appl. Phys. Lett. **86**, 011906 (2005).
[47] W. Lu, Z. Fan, Y. Yang, J. Ma, J. Lai, X. Song, X. Zhuo, Z. Xu, J. Liu, X. Hu *et al.*, Nat. Commun. **13**, 1623 (2022).
[48] X. C. Zhang, Y. Jin, K. Yang, and L. J. Schowalter, Phys. Rev. Lett. **69**, 2303 (1992).
[49] Z. Lei, Y. Huang, Z. Fan, W. Du, C. He, H. Wang, Y. Jin, and X. Xu, Appl. Phys. Lett. **116**, 161901 (2020).
[50] A. Reklaitis, J. Appl. Phys. **109**, 083108 (2011).
[51] K. Liu, J. Xu, T. Yuan, and X. C. Zhang, Phys. Rev. B **73**, 155330 (2006).
[52] F. V. Wald, J. Bullitt, and R. O. Bell, IEEE Trans. Nucl. Sci. **22**, 246 (1975).
[53] N. Laman, M. Bieler, and H. M. van Driel, J. Appl. Phys. **98**, 103507 (2005).
[54] L. Zhu, Y. Huang, Z. Yao, B. Quan, L. Zhang, J. Li, C. Gu, X. Xu, and Z. Ren, Nanoscale **9**, 10301 (2017).
[55] X. Lu, M. Qin, Y. Wang, J. Zhou, Q. Zhu, P. Peng, Y. Zhang, and H. Wu, Appl. Surf. Sci. **508**, 145219 (2020).
[56] E. H. Hwang, S. Adam, and S. Das Sarma, Phys. Rev. Lett. **98**, 186806 (2007).
[57] F. Xi, H. Yang, V. Khayrudinov, Y. He, T. Haggren, Y. Zhou, H. Lipsanen, Z. Sun, and X. Xu, Nanotechnology **33**, 085207 (2021).
[58] M. M. Glazov and S. D. Ganichev, Phys. Rep. **535**, 101 (2014).
[59] J. E. Sipe and A. I. Shkrebtii, Phys. Rev. B **61**, 5337 (2000).
[60] F. Blanchard, G. Sharma, L. Razzari, X. Ropagnol, H. Bandulet, F. Vidal, R. Morandotti, J. Kieffer, T. Ozaki, H. Tiedje *et al.*, IEEE J. Sel. Top. Quantum Electron. **17**, 5 (2011).
[61] Y. Guo, Q. Zhao, Z. Yao, K. Si, Y. Zhou, and X. Xu, Nanotechnology **28**, 335602 (2017).

[62] L. Braun, G. Mussler, A. Hruban, M. Konczykowski, T. Schumann, M. Wolf, M. Münzenberg, L. Perfetti, and T. Kampfrath, Nat. Commun. **7**, 13259 (2016).

[63] X. C. Zhang and D. H. Auston, J. Appl. Phys. **71**, 326 (1992).

[64] H. Koc, H. Ozisik, E. Deligöz, A. M. Mamedov, and E. Ozbay, J. Mol. Model. **20**, 2180 (2014).

[65] M. Medles, N. Benramdane, A. Bouzidi, A. Nakrela, H. Tabet-Derraz, Z. Kebbab, C. Mathieu, B. Khelifa, and R. Desfeux, Thin Solid Films **497**, 58 (2006).

[66] H. Moreno-García, M. T. S. Nair, and P. K. Nair, Thin Solid Films **519**, 2287 (2011).

[67] B. A. Hasan, Int. J. Adv. Sci. Tech. Res. **3**, 103 (2014).

[68] A. Yariv and P. Yeh, *Optical Waves in Crystals* (Wiley, New York, 1984).